Atomic Layer Deposition Process Modeling and Experimental Investigation for Sustainable Manufacturing of Nano Thin Films

Dongqing Pan[a], Dongsheng Guan[a], Tien-Chien Jen[b], Chris Yuan[a,*]

[a] Department of Mechanical Engineering, University of Wisconsin-Milwaukee, Milwaukee, WI 53201, USA

[b] Department of Mechanical Engineering Science, University of Johannesburg, Auckland Park, 2006, South Africa

*Corresponding author. Tel.: +1 414-229-5639; fax: +1 414-229-6958.

E-mail address: cyuan@uwm.edu (Chris Yuan).

This paper studies the adverse environmental impacts of atomic layer deposition (ALD) nano-manufacturing technology on ALD of Al_2O_3 nano-scale thin films. Numerical simulations with detailed ALD surface reaction mechanism developed based on Density Functional Theory (DFT), and atomic-level calculations are performed to investigate the effects of four process parameters including process temperature, pulse time, purge time, and carrier gas flow rate on ALD film deposition rate, process emissions and wastes. Full-cycle ALD simulations reveal that the depositions of nano-thin-films in ALD are in essence the chemisorption of the gaseous species and the conversion of surface species. Methane emissions are positively proportional to the film deposition process. The studies show that process temperature fundamentally affects the ALD chemical process by changing the energy states of the surface species. Pulse time is directly related to the precursor dosage. Purge time influences the ALD process by changing the gas-surface interaction time, and higher carrier gas flow rate alters the ALD flow field by accelerating the convective heat and mass transfer in ALD process.

Keywords: atomic layer deposition; density functional theory; sustainability; emissions; wastes

1 Introduction

As a vapor-phase additive nano-manufacturing technique with capabilities to deposit thin films with extremely uniform surface in atomic level, atomic layer deposition (ALD) has attracted extensive attentions from both academia and industry in the context of miniaturization of electronic devices driven by the consumer electronic products in recently years [1-3]. ALD has been extensively adopted in the microelectronics industries, and it is on rapid expansions to other cutting-edge fields, such as energy conversion and storage, medical and environmental health [4-9].

However, ALD was born with serious sustainability issues, especially for industrial-level applications. One is the low throughput defined by its nature of depositing material in atomic level. This issue has been extensively studied in our previous studies [10-13]. Another is the negative environmental impacts, largely due to the highly toxic chemicals used in ALD process, greenhouse gas emissions and nano-particle generations [14-16].

Taking Al_2O_3 ALD as an example, one of the common precursors, TMA, is extremely flammable and highly toxic, and can cause severe skin and eye damage [14, 15]. The un-reacted TMA molecules are purged out of the ALD system as one of the toxic wastes that pose a high risk to the public health and environment. The by-product, methane, is one of the major greenhouse gases [15]. Nano-particles can also be formed in ALD chamber, and the nano-particle emissions might be more hazardous to human health. These wastes and emissions may not be significantly noticeable in a few hundred deposition cycles in lab scale, but considering the large amount of dielectric materials demanded in the semiconductor industry, the amount of ALD wastes and emissions and their potentials to impact the environment can be seriously significant [15].

The previous studies show that ALD process features low material utilization efficiency. For instance, in Al_2O_3 ALD, only 50.4% of TMA is deposited on wafers revealed by experiments [14, 15]. ALD process is also shown highly energy-intensive. In Al_2O_3 ALD process, ~ 4.09 MJ energy is consumed for deposition of a 30 nm film [15]. Our previous experimental study on nano-particle emissions in Al_2O_3 ALD process shows that the total nano-particle emissions with diameter less than 100 nm are in the range of 6.0×10^5 and 2.5×10^6 particles in 25 cycles of Al_2O_3 ALD [16].

This paper focuses on the gaseous material wastes and emissions in the process of Al_2O_3

ALD. To be specific, the deposition process is characterized, and methane emissions in the process are investigated numerically and experimentally. The previously-established ALD numerical model is improved with detailed surface chemical kinetics and reaction mechanism achieved from DFT calculations [10]. The effects of four process parameters including temperature, pulse time, purge time, and carrier gas flow rate on deposition and material wastes and emissions are investigated systematically using the improved numerical model.

2 Al_2O_3 ALD Modeling with Detailed Chemical Kinetics

2.1 Physical Process Modeling

As a vapor film fabrication technique, ALD is a strongly-coupled physical and chemical process. The physical thermal-fluid process of ALD includes momentum transport, mass transport and heat transfer. The modeling process is described in great detail in our previous papers [10, 11, 13]. The mathematical modeling equations are listed as follows.

$$\frac{\partial \rho}{\partial t} + \nabla \cdot (\rho \vec{V}) = 0 \tag{1}$$

$$\frac{\partial}{\partial t}(\rho \vec{V}) + \nabla \cdot (\rho \vec{V}\vec{V}) = -\nabla p + \nabla \cdot \bar{\bar{\tau}} + \rho \vec{g} + \vec{F} \tag{2}$$

$$\frac{\partial}{\partial t}(\rho c_i) + \nabla \cdot (\rho c_i \vec{V}) = -\nabla \cdot \vec{J}_{m,i} + R_i \tag{3}$$

$$\frac{\partial}{\partial t}(\rho E) + \nabla \cdot [\vec{V}(\rho E + p)] = \nabla \cdot [k \nabla T - \sum_i h_i \vec{J}_{h,i} + (\bar{\bar{\tau}} \cdot \vec{V})] \tag{4}$$

where ρ is the density, $\vec{V}$ is the velocity vector, p is the static pressure, $\rho \vec{g}$ and $\vec{F}$ are the gravitational body force and external body forces, respectively; $\bar{\bar{\tau}}$ is the stress tensor, c_i is the local molar fraction of species i, R_i is the net rate of production of species i by chemical reaction, $\vec{J}_{m,i}$ is the mass diffusive flux of mixture species i, k is the material thermal conductivity, h_i is the enthalpy of mixture species i, and $\vec{J}_{h,i}$ is the energy diffusive flux of mixture species i.

The continuity equation (1) conserves mass. The Navier-Stokes equations (2) are adopted to model the process of momentum transport in the gaseous flow of ALD reactor. The species

transport process is governed by the convection-diffusion equation (3), which is coupled by the chemical kinetics. The energy equation (4) is modeling the overall heat transfer in ALD reactor. The detailed numerical model setup including the 3D geometry, meshing, and boundary condition definitions can be found in our previous papers [10-12]. In this paper, more modeling endeavors are invested in the improvement of reaction mechanism and chemical kinetic model.

2.2 Surface Reaction Modeling

The surface chemical kinetics of ALD is of critical importance to characterize the film deposition process, emissions and wastes. However, it is extremely challenging to obtain the detailed information regarding the surface reactions in atomic level by in-situ experimental characterizations [17]. With great capabilities to obtain the energetic and structural information about the molecular interactions that are essential to understand chemical reactions, computational quantum chemistry approaches such as DFT method provide a satisfactory alternative to study the ALD surface reaction mechanism and pathway [17]. Quite a few studies regarding the molecular interactions of Al_2O_3 ALD using DFT methods have been reported [17-23]. This paper takes advantage of these DFT reaction calculations and chemical kinetic data to improve our numerical ALD model.

The overall Al_2O_3 ALD using TMA and water can be expressed as,

$$2Al(CH_3)_3^{\,g} + 3H_2O^{g} \rightarrow Al_2O_3^{\,b} + 6CH_4^{\,g} \quad (5)$$

where superscripts g and b represent gas and bulk (solid) species, respectively. This overall reaction equation cannot be directly used in the chemical kinetic model because it reveals nothing regarding the actual ALD pulse process in Al_2O_3 ALD.

A more complex chemisorption reaction mechanism in Al_2O_3 ALD depicting the actual sequencial ALD pulse and reaction steps is modeled by following two half reactions:

$$2Al(CH_3)_3^{\,g} + 3OH^{*} \rightarrow Al\text{-}CH_3^{\,*} + Al\text{-}(CH_3)_2^{\,*} + 3O^{b} + 3CH_4^{\,g} \quad (6)$$

$$3H_2O^{g} + Al\text{-}CH_3^{\,*} + Al\text{-}(CH_3)_2^{\,*} \rightarrow 3OH^{*} + 2Al^{b} + 3CH_4^{\,g} \quad (7)$$

where superscripts * represents surface site species. These two irreversible equations reveal the actual Al_2O_3 ALD reaction sequences, and with suffient chemical kinetic information, this mechanism is proper to simplify and approximate the actual suface reaction and material

deposition processes in ALD reactors [10]. However, the above two half reactions hardly include the knowledge regarding the elementary reaction steps as well as the kinetic information of ALD process, which are specially important to model the process wastes and emissions.

With the aid of detailed DFT quantum chemistry calculations, much more detailed chemical deposition mechanism and pathway of Al_2O_3 ALD are proposed as illustrated in the following section [17-23].

For the substrate surface initiations, in both our numerical and experimental settings, we use silicon as substrate, and materials are deposited on the Si (100) surface. In DFT studies, Si_9H_{12} cluster is used to investigate the chemical reactivity and vibrational properties of the Si (100) surface [19].

Regarding the the initial suface species in Al_2O_3 ALD, Delabie et al. studied the possible CH_3 and OH terminated surface species on silicon surface using DFT approach [21]. The cited work shows that the hydrolysis of the $SiCH_3$ is kinetically unfavorable due to the five coordinated Si atoms in the transition state structure, which makes the following surface reation with water extremely difficult [21]. Their studies imply that in actual Al_2O_3 ALD, it is unlikely to have methyl-covered surface on Si (100) surface. Meanwhile, OH-terminated Si (100) surface reacting with TMA results in experimentally consistent results. It is reasonable to presume that the silicon surface is hydroxylated with OH groups initially.

In TMA pulse step, with OH-terminated silicon suface, the ALD deposition begins by interacting with gaseous TMA molecules forming a bond between O and Al atoms [17-19]. The formation is reversible and generates an intermediate surface species as shown in Reaction R1.

$$\text{R1:Al}(CH_3)_3^{g} + \underset{\wedge}{O}H^{*} \underset{b}{\overset{f}{\hat{U}}} (CH_3)_3Al\underset{\wedge}{O}H^{*} \qquad (8)$$

where f and b represent the forward and backward reactions, respectively, and the symbol ^ denotes the surface bond linkage with surface group.

The above intermediate surface group $(CH_3)_3Al\underset{\wedge}{O}H^{*}$ further proceeds to a transition state structure by forming a bond between the O atom and an H atom from one of the three methyl ligands, and finally evolves to a more stable structure with two methyl-terminated ligands by releasing a methane molecule. This process is represented by Reaction R2.

$$R2: (CH_3)_3Al\underset{\wedge}{O}H^* \hat{U} \ (CH_3)_3Al\underset{\wedge}{O}H^{\ddagger} \triangleright \ (CH_3)_2Al\underset{\wedge}{O}^* + CH_4{}^g - \qquad (9)$$

where the superscript ‡ represents the transition state. The energy profiles of these two reactions can be found in the cited paper [19] . The emission of gaseous methane makes this process irreversible.

The energy profile of DFT study [19] shows that the formed surface species $(CH_3)_2Al\underset{\wedge}{O}^*$ is in high energy state, and is kinetically inclined to interact with the nearby OH* group resulting an intermediate surface group as shown in following reaction, R3,

$$R3: (CH_3)_2Al\underset{\wedge}{O}^* + \underset{\wedge}{O}H^* \hat{U}_b^f \ (CH_3)_2Al\underset{\wedge}{O}_2H^* \qquad (10)$$

In the complex of $(CH_3)_2Al\underset{\wedge}{O}_2H^*$, a linkage between the Al atom and the hydroxyl O atom is formed. A transition structure is readily formed when the stand-alone hydroxyl H atom is attached to one of the two methyl ligands. As a result, a methane molecule is emitted as shown in Reaction R4.

$$R4: (CH_3)_2Al\underset{\wedge}{O}_2H^* \hat{U} \ (CH_3)_2Al\underset{\wedge}{O}_2H^{\ddagger} \triangleright \ CH_3Al\underset{\wedge}{O}_2{}^* + CH_4{}^g - \qquad (11)$$

At this point, much more stable species $AlCH_3$* indicated by the energy profile terminates the surface species evolutions in TMA pulse step. The initial OH-terminated substrate surface in R1 is transformed to Al $(CH_3)_2$* by R2, and $AlCH_3$* by R4, leaving O and Al atoms anchored in the formed surface structures. Since the double-methyl-mounted species (Al $(CH_3)_2$*) is kinetically unstable, the most part of the final substrate surface after TMA pulse is covered by $AlCH_3$* with only a smaller number of Al $(CH_3)_2$*.

For water pulse step, due to the coexistence of the two possible methyl-terminated surface species, the surface reaction mechanism is two-fold. In the case of the double-methyl-terminated species Al $(CH_3)_2$*, a water molecule is chemisorbed by the Al atom resulting two stand-alone H atoms as shown in Reaction R5. One of the H atoms is attracted by the C atom of the methyl group resulting in a temporary O-H-C linkage. The transitional bond is finally broken at the O-H bond leaving the surface site terminated with a heterogeneous mixture of OH and CH_3. Presented in Reaction R6, a methane molecule is emitted in the process.

$$R5: (CH_3)_2Al\underset{\wedge}{O}^* + H_2O^g \hat{U}_b^f \ (CH_3)_2\underset{\wedge}{O}AlOH_2{}^* \qquad (12)$$

$$\text{R6: } (CH_3)_2\underset{\wedge}{O}AlOH_2^{*} \hat{U} \ (CH_3)_2\underset{\wedge}{O}AlOH_2^{\ddagger} \text{ Þ } CH_3\underset{\wedge}{O}AlOH^{*} + CH_4^{g} \text{ -} \qquad (13)$$

Contacting with another water molecule, the surface site further evolves to an intermediate structure denoted as $CH_3\underset{\wedge}{O}AlOHOH_2^{*}$ shown in the following Reaction R7. A transition state structure is further generated in R8 when a similar transitional O-H-C bond is formed. The transition state structure $CH_3\underset{\wedge}{O}AlOHOH_2^{\ddagger}$ is the barrier before reaching the final stable OH-terminated structure.

$$\text{R 7: } CH_3\underset{\wedge}{O}AlOH^{*} + H_2O^{g} \underset{b}{\overset{f}{\hat{U}}} \ CH_3\underset{\wedge}{O}AlOHOH_2^{*} \qquad (14)$$

$$\text{R8: } CH_3\underset{\wedge}{O}AlOHOH_2^{*} \hat{U} \ CH_3\underset{\wedge}{O}AlOHOH_2^{\ddagger} \text{ Þ } \underset{\wedge}{O}Al(OH)_2^{*} + CH_4^{g} \text{ -} \qquad (15)$$

With breakage of the transitional bond, a methane molecule is generated, which leaves the surface sites fully covered by two OH groups. The structure has no more place for extra water molecules, and the transformation of the double-methyl-terminated species Al $(CH_3)_2$* to double-hydroxyl-terminated species $Al(OH)_2^{*}$ is finalized.

The process of single-methyl-terminated species $AlCH_3$* interacting with water molecules is similar and presented in the following Reactions R9 and R10.

$$\text{R 9: } \underset{\wedge}{Al}CH_3^{*} + H_2O^{g} \underset{b}{\overset{f}{\hat{U}}} \ CH_3\underset{\wedge}{Al}OH_2^{*} \qquad (16)$$

$$\text{R10: } CH_3\underset{\wedge}{Al}OH_2^{*} \hat{U} \ CH_3\underset{\wedge}{Al}OH_2^{\ddagger} \text{ Þ } \underset{\wedge}{Al}OH^{*} + CH_4^{g} \text{ -} \qquad (17)$$

Water molecule is firstly adsorbed by the Al atom resulting in an intermediate species denoted as $CH_3\underset{\wedge}{Al}OH_2^{*}$. With extra energy, the species further evolves into a transition state structure by forming the O-H-C bond. The excited structure is finally transformed to a single-hydroxyl-terminated species by emitting a methane molecule. During the process, an extra Al-O is formed.

As described in the above deposition reactions R1-R10, the ALD deposition process is actually involved with the transformations of different surface species. TMA pulse leaves the substrate surface with O-Al bonds and methyl-terminated surface sites, which are further converted in water pulse by forming Al-O bonds leaving the surface covered by hydroxyl-terminated sites. Within one ALD cycle, the silicon surface is reconstructed with the O-Al-O bonds which reprensents a single layer of Al_2O_3 film. Revealed by the DFT energy profiles of the mechanism [18-22], the success of these atomic-level transformations heavily

depends on the energy conditions, the availability of gaseous species and surface species. The reaction conditions are defined by the macro-level process parameters, such as the temperature, precursor distributions.

2.3 Physical and Chemical Model Coupling

With the above detailed reaction mechanism and pathway, the chemical kinetics of Al_2O_3 ALD is coupled with the thermal-fluid dynamics model by chemical kinetics rate law [24]. The reaction rate $\hat{A}_r$ (mol/m^3·s) of rth surface reaction R_r is obtained by the chemical rate equation(19).

$$R_r: \sum_{i=1}^{N_g} g_i' G_i + \sum_{i=1}^{N_b} b_i' B_i + \sum_{i=1}^{N_s} s_i' S_i \overset{k_f}{\underset{k_b}{\hat{U}}} \sum_{i=1}^{N_g} g_i'' G_i + \sum_{i=1}^{N_b} b_i'' B_i + \sum_{i=1}^{N_s} s_i'' S_i \tag{18}$$

$$\hat{A}_r = k_f \prod_{i=1}^{N_g} [G_i]_w^{g_i'} \prod_{j=1}^{N_s} \theta_{S_j}^{s_j'} \tag{19}$$

where, G, B, and S are gaseous, bulk and surface species, g_i', b_i' and s_i' are the stoichiometric coefficients for the ith species as a reactant, g_i'', b_i'' and s_i'' are the stoichiometric coefficients for the ith species as a product. N_g, N_b and N_s are the number of gaseous, bulk and surface species involved in that specific reaction. $[\ ]_w$ represents surface coverage of surface species and concentrations of gaseous species on the wafer surface, respectively.

For an irreversible reaction, the reaction rate constant of rth surface reaction is determined by the Arrhenius expression,

$$k_r = A \exp\left(\frac{E_a}{RT}\right) \tag{20}$$

where A is the pre-exponential factor, E_a is the activation energy, T is temperature in K, and R is the universal gas constant.

The pre-exponential factor, also known as the frequency factor represents the frequency of collisions between reactant molecules. It is practically unfeasible to obtain the pre-exponential factor empirically by experiments, and the collision theory estimation is not accurate for gas-solid surface interactions [25, 26]. However, the transition state theory gives more accurate representation of the pre-exponential factor through the Eyring equation [26]. Detailed derivations of the following expression for pre-exponential factor can be found in the

cited literatures [26, 27].

$$A = \left(\frac{k_B T}{h}\right) \exp\left(\frac{\Delta S_0^{\ddagger}}{R}\right) \tag{21}$$

where h and k_B are Planck's constant and Boltzmann's constant, respectively. $\Delta S_0^{\ddagger}$ is the change in standard entropy of forming the transition state.

The activation energy in Arrhenius expression is the change in standard enthalpy of forming the transition state as following,

$$E_a = \Delta H_0^{\ddagger} \tag{22}$$

The activation energy is the energy barrier which can be characterized from the energy profiles achieved from DFT calculations, while entropy change $\Delta S_0^{\ddagger}$ is evaluated through the equilibrium constant of forming the transition state, which is expressed as [27],

$$\Delta S_0^{\ddagger} = R \ln K^{\ddagger} + \frac{\Delta H_0^{\ddagger}}{T} \tag{23}$$

where the equilibrium constant is computed using statistical mechanics methods and the molecular partition functions [17].

The backward reaction constant k_b in the ALD reversible reactions are evaluated by the equilibrium constant K,

$$k_b = \frac{k_f}{K} \tag{24}$$

The equilibrium constants pertaining to these ALD reactions are listed in the cited reference [17].The reaction energy data such as change of enthalpy can be found in the cited DFT studies [18-22].

With the improved ALD chemical kinetic model, three levels of four process parameters, temperature (150°C, 200°C and 250°C), pulse time (0.015, 0.02, and 0.025 s), purge time (5, 10 and 15 s) and carrier gas flow rate (10, 20 and 30 sccm) are simulated to study their effects on the surface depostion, process wastes and emissions.

3 Experiments

Based on the same ALD system in the numerical model, experiments of characterizing the surface reaction process and emissions in Al_2O_3 ALD are carried out in the Cambridge

NanoTech Savannah 100 ALD reactor. To benchmark the numerical model especially the chemical kinetics in terms of film growth rate, Al_2O_3 films are deposited on substrates of Si using 99.9% TMA and 99.0% distilled water under three levels of deposition temperatures, 150°C, 200°C and 250°C. The ALD cycle starts with 300 seconds stabilization, followed by 0.02 s pulse and 10 s purge procedures for both TMA and water. The Al_2O_3 films are deposited with 500 cycles, and the film thickness is characterized by the UVISEL Spectroscopic Ellipsometer (HORIBA, Ltd.).

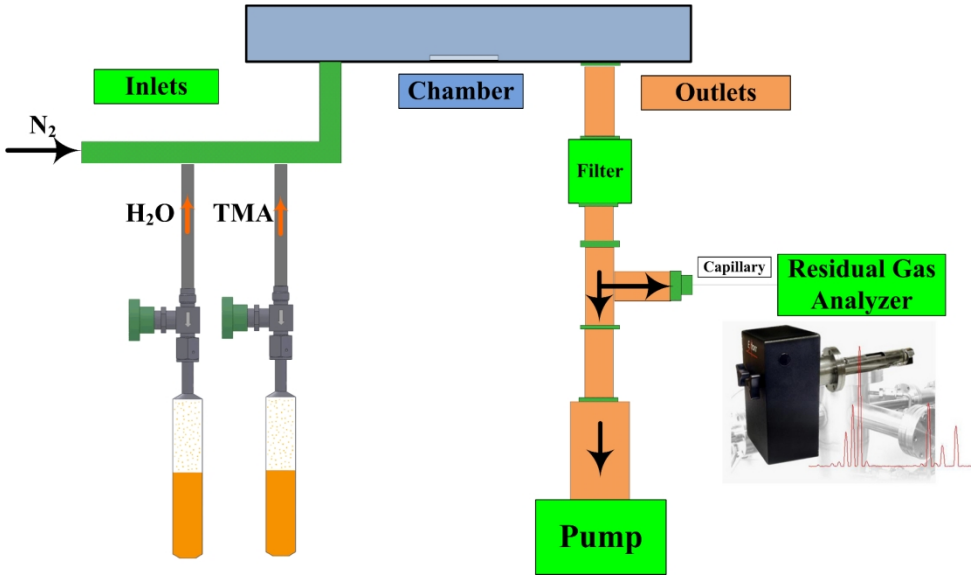

Fig.1 Experimental ALD system with residual gas analyzer (RGA) to characterize the methane emissions

Spectroscopic ellipsometry is an optical technique to characterize the dielectric properties of thin films, e.g., complex refractive index or dielectric function. Typically, the information about the composition, roughness, thickness (depth), crystalline nature, doping concentration, electrical conductivity and other material properties of thin films can be achieved through ellipsometry.

The UVISEL Spectroscopic Ellipsometry system used in our study is operated by measuring the change in polarization of the incident radiation (with spectral range of 190-2100 nm in the UVISEL system) after interacting (reflection, absorption, scatter, or transmission) with the sample thin films. Since the detected signal is dependent of thickness as well as the film properties, ellipsometry is an excellent tool to determine of thickness and optical constants of thin films [28]. The UVISEL Spectroscopic Ellipsometer used in this study is capable to measure thin film thickness from 1Å to 45 μm with high precision, sensitivity, and resolution.

In the proceeding of ALD cycles, an in-situ gas analyzer is used to characterize methane

emissions in Al_2O_3 ALD as shown in the scheme of Fig.1. Precursors stored in separate cylinders are injected sequentially into the ALD chamber when the corresponding ALD valve is open. Si wafers with 10 mm by 20 mm are placed in the center of the chamber. A residual gas analyzer (Extorr XT Series RGA) is connected in the outlet after a gas particulate filter with 100 nm pore size filter element. RGA is a type of mass spectrometer based on quadrupole technology for process control and contamination monitoring, and typically used in high vacuum systems, e.g., $\sim 1\times10^{-7}$ torr in the Extorr XT 100 RGA system used in our experiments. It measures the pressure of gases by sensing the weight of each atom as they pass through the quadrupole mass analyzer. RGA is capable to characterize the chemical species involved in gas phase reactions, and it can be used to monitor the stability of the gas environment.

The Extorr XT 100 RGA system can detect gases with mass up to 100 amu as well as their concentrations. The emissions are sampled through a capillary tube into the RGA device. In our specific experimental setup, due to the possible condensation of water vapor in the cooler outlet and RGA tubing, and considering the possible reactions of TMA waste with the condensed water, it is extremely difficult to accurately characterize either TMA waste or water vapor in our ALD system. In our experiments, we particularly focus on methane emissions.

4 Results and Discussions

4.1 Al_2O_3 ALD Deposition Process

Using the reaction mechanism and the chemical kinetic model, a full cycle of Al_2O_3 ALD with 0.02 s pulse and 10 s purge is simulated with the chamber temperature 200°C. The contour plots of gaseous species distributions and the bulk species deposition rates in the entire ALD system are presented in Fig. 2 (a) and (b) at the end of the two pulse steps, 0.02 s and 10.04 s, respectively, and Fig.3 shows the gaseous species distributions in the full ALD cycle with the data probed in the center area of the ALD chamber.

At the initial state, only carrier gas N_2 exists in the chamber. As the ALD valve is open for TMA pulse, TMA concentration increases steadily, while N_2 concentration decreases as seen in Fig.3. The increasing methane concentration shows the surface reaction is activated and material deposition is initiated. Methane concentration reaches its peak during the 0.02 s pulse step and declines slightly after that. The declined methane concentration is mainly due to the

fact that the reaction rate decreases as the reactive surface sites OH* is being consumed.

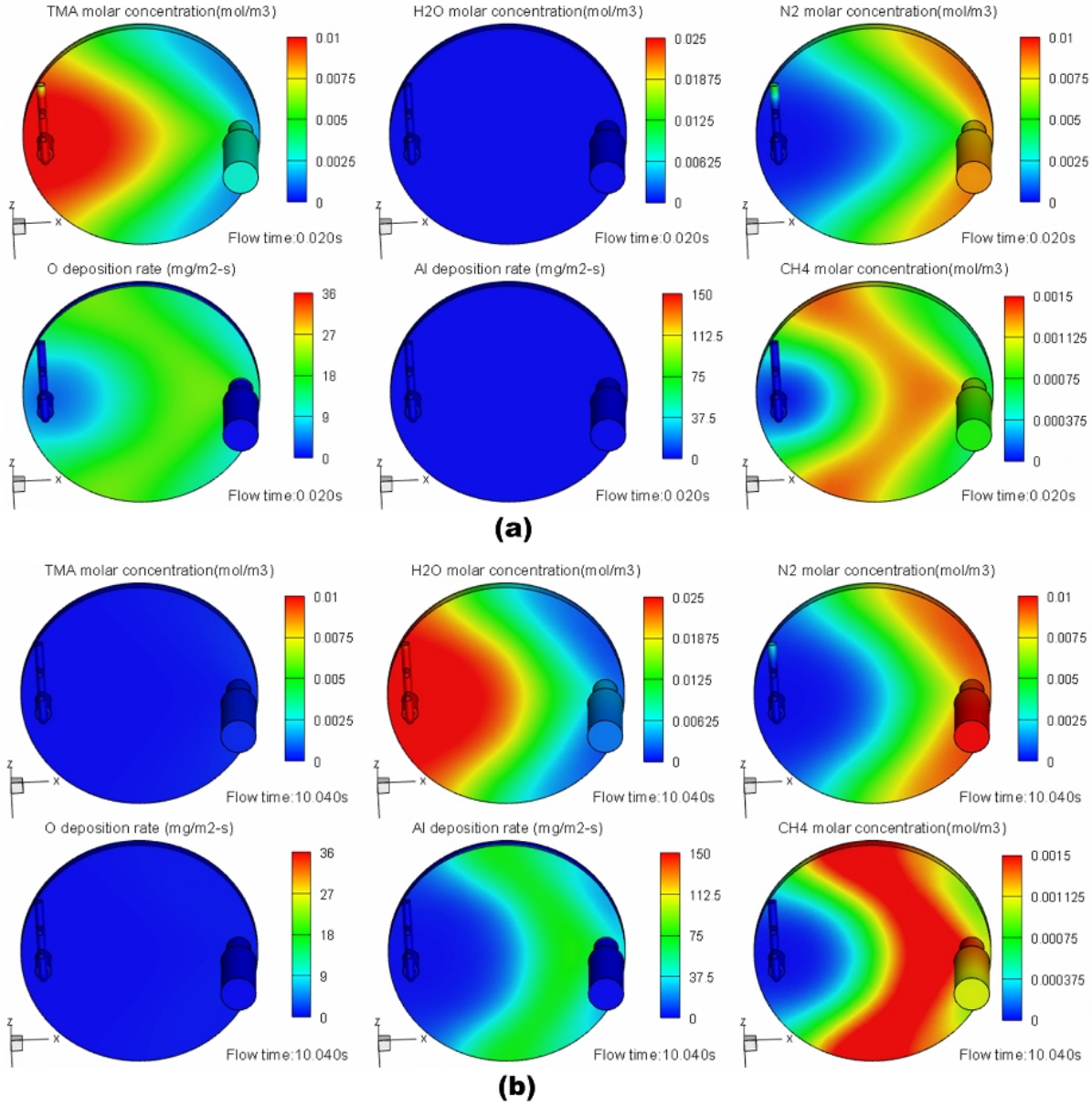

Fig.2 Contour plots of gaseous species distributions and the bulk species deposition rates (a) 0.02 s at the end of TMA pulse and (b) 10.04 s at the end of water pulse

Methane generation rate is further decreased as the TMA pulse process ends. As TMA concentration declines during the purge step, the low level of methane concentration in the center area of chamber is maintained by the TMA residuals during the first half of purge step. The increasing carrier gas concentration shows that N_2 dominates the chamber space again during the purge step. The materials are not evenly distributed in the entire ALD geometry, and along the flow field, the inlet area encounters the precursor flow first as shown in Fig.2.

The material concentration in water pulse process has the similar variations as seen in TMA pulse step. As water is being injected into the chamber, methane concentration increases steadily and reaches a higher peak. In the second purge process, as water concentration

declines promptly, much less methane can be detected in the center area. The gaseous material distribution variations in the center area are profoundly related to the surface species coverage as presented in Fig.4.

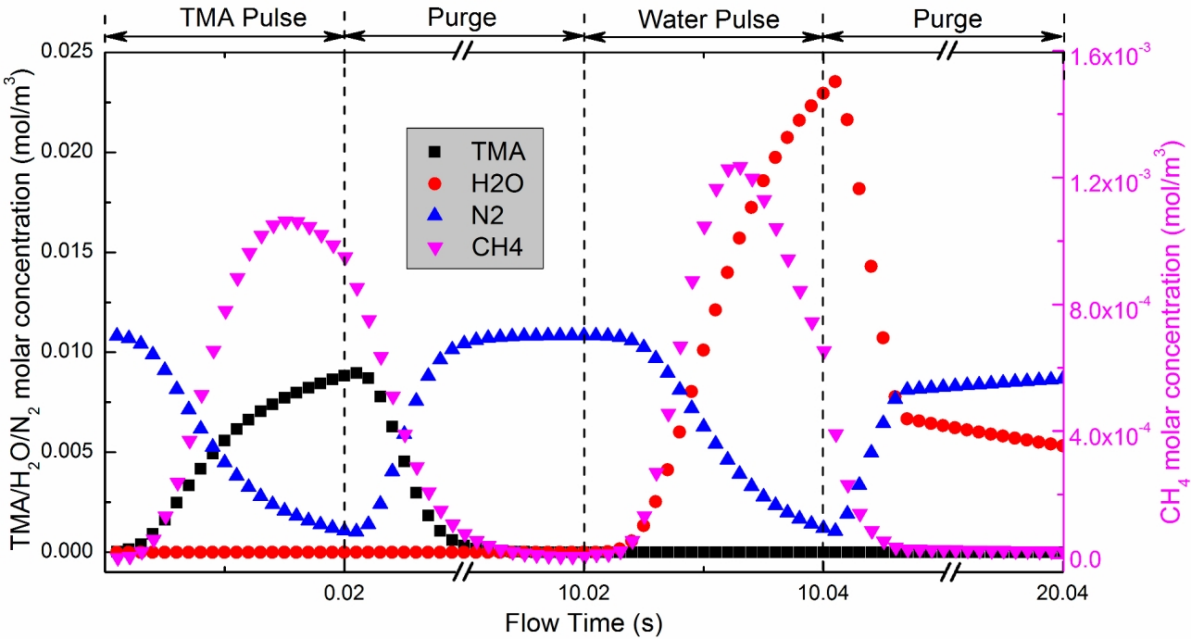

Fig.3 Gaseous species distributions during the full ALD cycle

The contour plots of surface coverage and precursor distributions in the entire ALD system for TMA and water pulse steps are shown in Fig.5 (a) and (b), respectively. A full coverage of OH* is assumed initially, and its coverage declines slightly in the first few milliseconds as shown in Fig.4, and deceases promptly following that, until it reaches ~ 20% at the end of the TMA pulse step. To be specific, 21.8% OH* species is left on the surface, and is further consumed in the following purge step. This indicates that within TMA pulse step, the surface reactions are not saturated as also shown by the contour plots in Fig.5 (a), especially in the outlet area. Part of surface reaction is completed during the following purge step.

Meanwhile, the two types of methyl-terminated species, Al $(CH_3)_2$* and $AlCH_3$* are being generated on the surface. At the end of TMA pulse step as shown in Fig.5 (a), the majority of the surface area is covered by $AlCH_3$* (~ 77.5% in the center area), while only ~ 1.7% is covered by Al $(CH_3)_2$*. Other intermediate surface species involved in R1-R10 has much lower level coverage (in the level of 10^{-6}) as indicated in Fig.5. This is consistent with conclusion from DFT studies that Al $(CH_3)_2$* is not stable [19]. At the end of the first purge step, 98% substrate surface in the center area is covered by $AlCH_3$* and less than 2% is

covered by Al $(CH_3)_2$*. In water pulse, both methyl-terminated surface species are converted back to OH* species as shown in Fig.4 and Fig.5 (b). At the end of pulse process, ~ 96.7% surface sites are covered by hydroxyl-terminated species. A very small portion of surface reactions are completed in the second purge step.

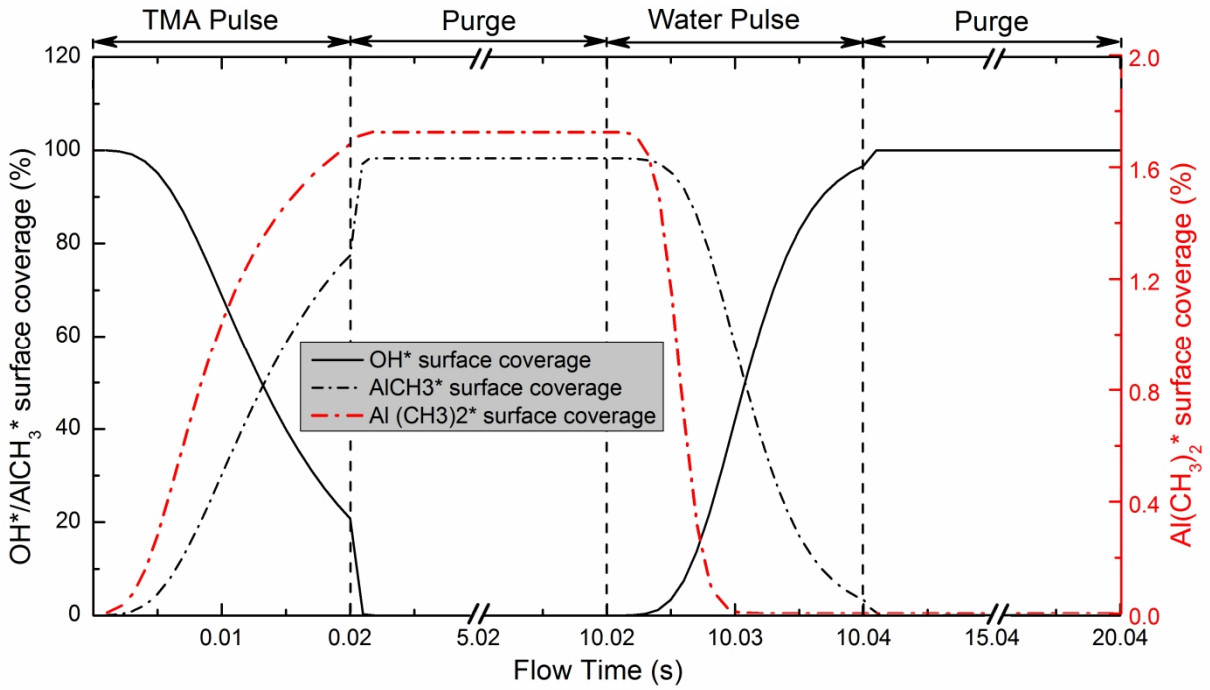

Fig.4 Surface coverage for the main surface species during the full ALD cycle

Figure 6 presents the bulk species deposition rate correlated with precursor concentrations during the full ALD cycle in the center area. It's found that the bulk species deposition rate is proportional to the corresponding precursor concentration. As shown in Fig.6, both of the Al and O deposition rates take the parabolic shape with peak values in the pulse process. This is due to the fact that deposition process is not only dependent on the gaseous species concentration, but also influenced by the reactive surface species. Although the precursor concentrations are increasing during the pulse steps, the increased deposition rate is balanced by the deceasing reactive surface sites.

Together with the analysis of the elementary chemical reactions in the previous section, the full-cycle ALD simulations confirm that the processes of the chemisorption of the gaseous species and conversion of the surface species bulk material depositions in ALD. Accompanying the deposition process, methane emissions are generated, and process wastes are released. The actual deposition process is heavily dependent on interactions of the gaseous, surface and bulk species, which are essentially influenced by the process parameters such as temperature, pulse and purge procedures as well as the carrier gas flow rate. In the section that

follows, these influential factors are investigated systematically.

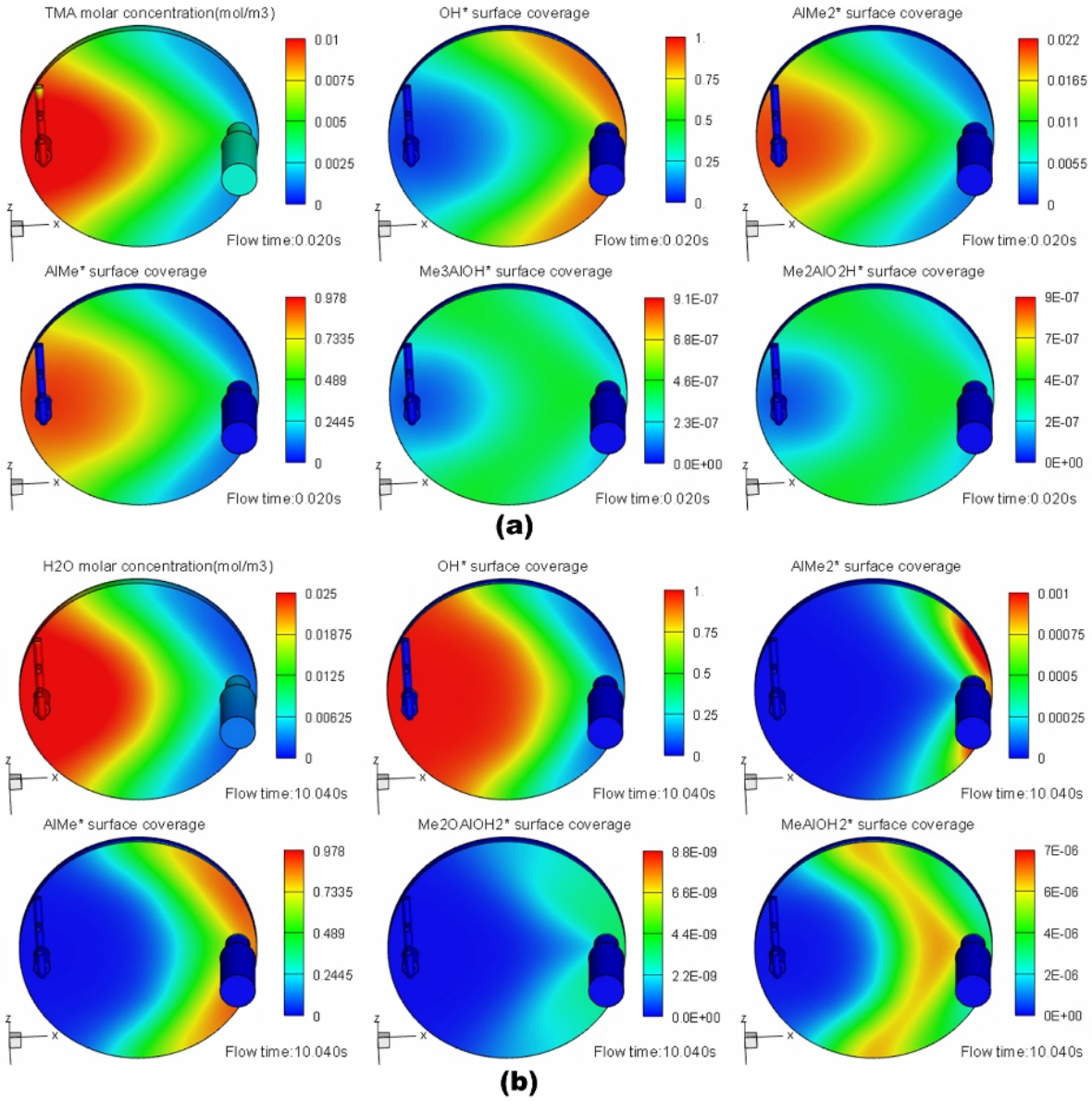

Fig.5 Contour plots of surface coverage and precursor distributions in the entire ALD system (a) 0.02 s at the end of TMA pulse and (b) 10.04 s at the end of water pulse

4.2 Effects of Process Parameters on ALD Wastes and Emissions

In this section, the four process parameters, temperature, pulse time, purge time, and carrier gas flow rate are specially investigated to explore their effects on the gaseous wastes and emissions. The objective of the effect studies is to minimize the negative environmental impacts such as wastes and emissions while maintaining a high material deposition rate in the concerned ALD process.

Temperature is an essential factor in ALD chemical process defined in the Arrhenius equation(20). Same as experimental settings, the inlet and outlet tubing of numerical model is

heated to 150°C, and chamber temperature is adjusted in three levels of 150°C, 200°C and 250°C. The effects of chamber temperature on total precursor dosage, precursor wastes and methane emissions are presented in Fig.7 with 0.02/10/0.02/10 s ALD cycle and 30 sccm carrier gas flow rate. The experimental results are also plotted in Fig.7 to benchmark the numerical results. It is found that precursor dosage is barely affected by the process temperature. In fact, precursor dosage is mainly determined by the pressure difference between precursor cylinder and the vacuum chamber, which is rarely influenced by the chamber temperature [10].

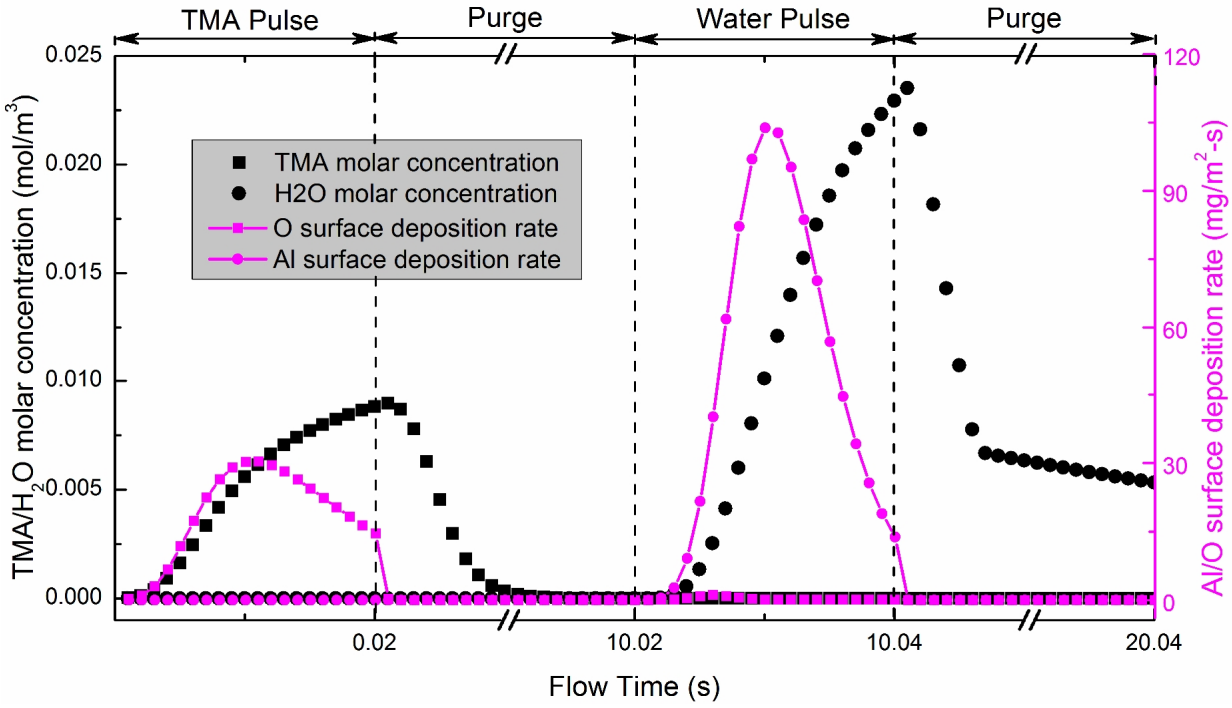

Fig.6 Correlation of the bulk species deposition rate and precursors concentration during the ALD cycle

As described in the reaction mechanism, methane emissions are closely pertinent to the deposition process. The actual ALD involves both chemisorption and desorption or decomposition (backward reactions). Higher temperature of 200°C accelerates both chemisorption and desorption, but the overall effect as shown by the results in Fig.7 is the enhancement of chemisorption process. As a result, methane emissions are increased as shown in Fig.7 (a) from 150°C to 200°C. This is consistent with the film growth rate presented in Fig.7 (b). When the chamber is further heated to 250°C, however, the growth rate is shown decreased in both experimental and numerical results.

This is largely due to the fact that the enhanced desorption process dominates over the chemisorption at higher temperature of 250°C. Taking Reactions R1 and R5 as examples, the extra energy at 250°C in the system can be sufficient to overcome the energy barriers of the

reverse reactions which are 0.6 eV and 0.85 eV for R1 and R5, respectively [19]. This leads to the breakage of the formed O-Al bond in R1 and Al-O bond in R5.

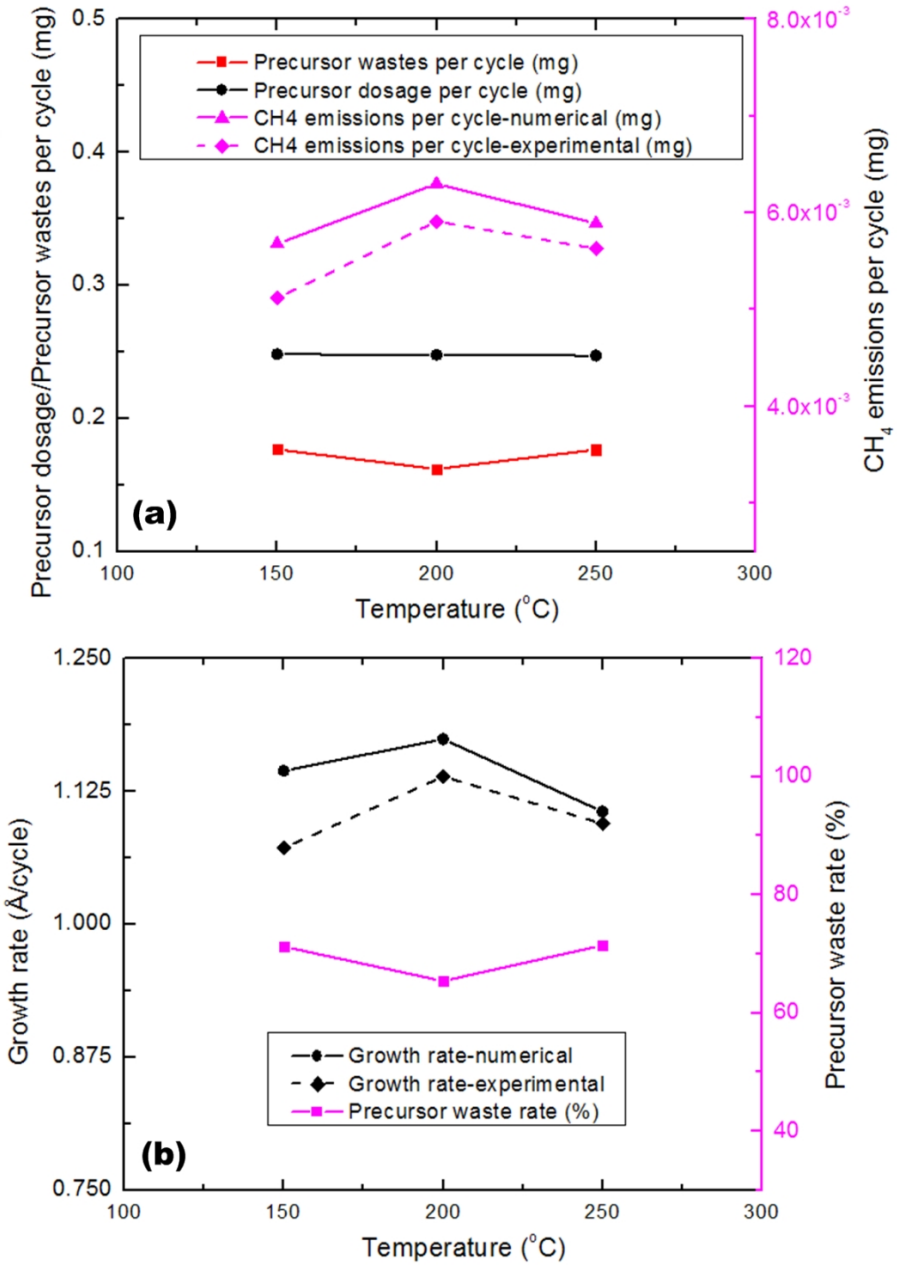

Fig.7 Effects of chamber temperatures on the process wastes and emissions (a) precursor dosage, precursor wastes and methane emissions and (b) film growth rate and precursor waste rate

With the enhanced desorption process, surface reactions cannot proceed to form O or Al atom depositions on the substrate surface, and as an undesirable result, the precursor molecules are returned to chamber and purged out as wastes. As shown in Fig.7 (a), the total precursor wastes are increased at 250°C from 200°C. Presented in Fig.7 (b), the precursor wastes are reversely related to the deposition rate.

The experimental data of methane emissions in 500 cycles of depositions are also plotted

to benchmark the numerical results in Fig.7. As an overall remark on the effects of temperature in terms of material deposition, wastes and emissions, the results show that at moderate temperature of 200°C, more precursors are utilized for film depositions with the lowest precursor waste rate (65.4%), and in the meantime, the highest growth rate of 1.17 Å/cycle is achieved.

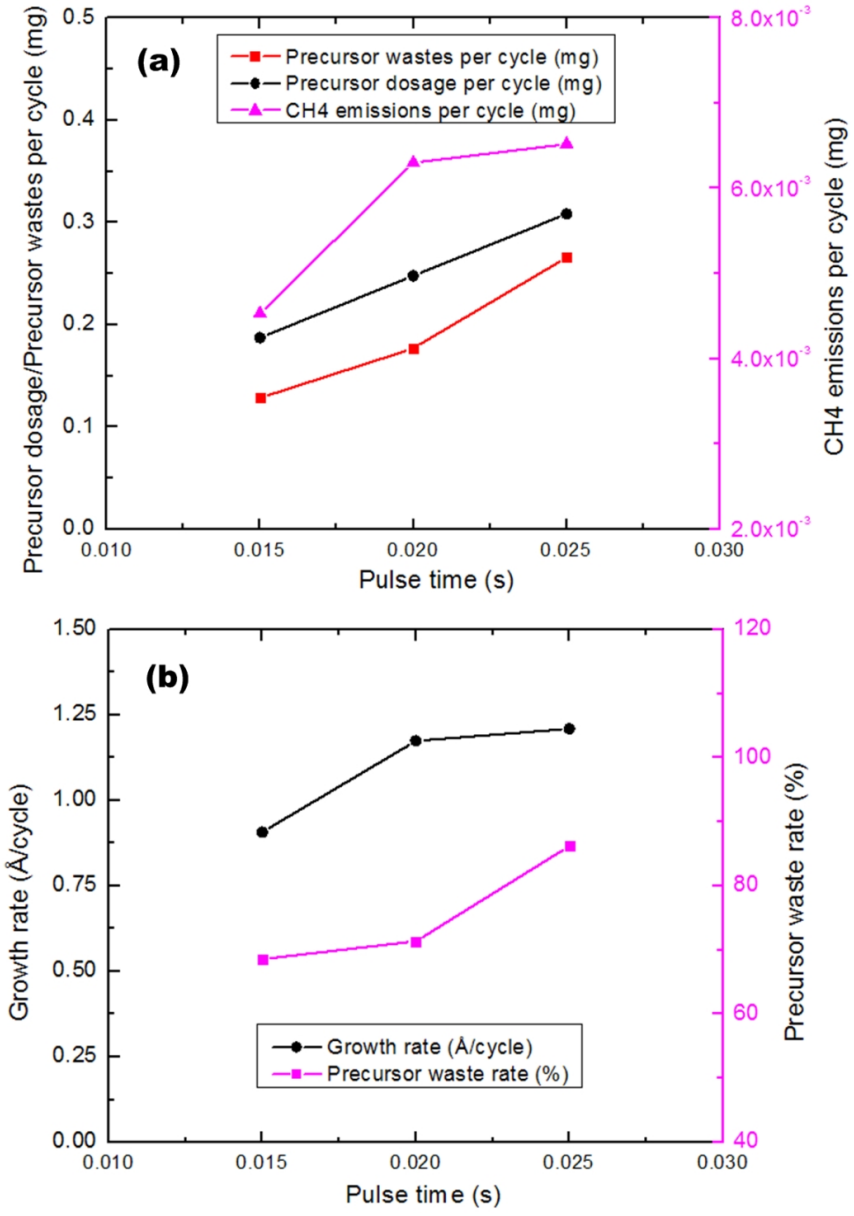

Fig.8 Effects of pulse time on the process wastes and emissions (a) precursor dosage, precursor wastes and methane emissions and (b) film growth rate and precursor waste rate

Precursor dosage is directly proportional to the pulse time as shown in Fig.8, in which ALD process is simulated at three levels of pulse time 0.015 s, 0.02 s and 0.025 s with 10 s purge time at 200°C and 30 sccm carrier gas flow rate. Driven by the pressure difference, the precursor dosage in one ALD cycle is increased from 0.187 mg to 0.308 mg as pulse time is

prolonged from 0.015 s to 0.025 s. With more precursor molecules injected into the reactor, the reactions are driven to the forward direction, and the reverse reactions are restrained, which results in more material depositions and methane generations. As shown in Fig.8 (a), methane emissions per cycle are increased from 4.5×10^{-3} mg to 6.3×10^{-3} mg, and meanwhile, the growth rate presented in Fig.8 (b) is significantly increased from 0.91 Å/cycle to 1.17 Å/cycle when the pulse time is increased to 0.02 s from 0.015 s.

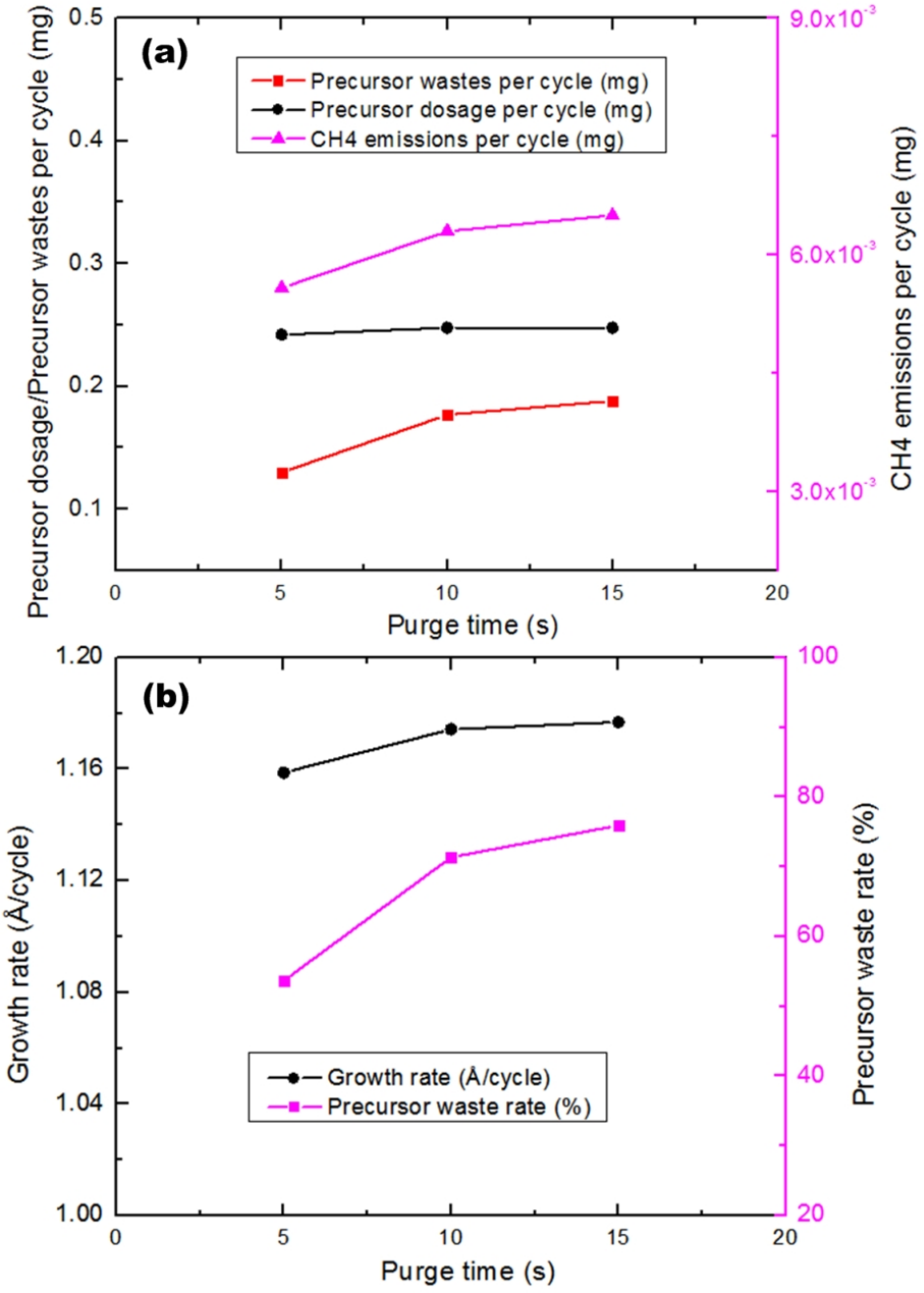

Fig.9 Effects of purge time on the process wastes and emissions (a) precursor dosage, precursor wastes and methane emissions and (b) film growth rate and precursor waste rate

When pulse time is further increased to 0.025 s, slight increments are seen for both methane emission and growth rate. In the case of 0.025 s pulse time when too much precursor

is supplied to the substrate surface, the extra materials cannot be absorbed in a limited time, and are finally purged out of the system due to the possible saturation of the surface reactions. As revealed in Fig.8 (a), a significant increment of precursor wastes is observed at 0.025 s pulse. In such a condition, precursors are greatly overdosed, and this seriously deteriorates the sustainability performance of ALD. As presented in Fig.8 (b), the precursor waste rate is as high as 86.2% at 0.025 s pulse time compared to 70% of 0.02 s. Fewer precursor is wasted at 0.015 s pulse time, but the growth rate is low, only 0.91 Å/cycle as shown in Fig.8 (b). As a trade-off, 0.02 s is the optimal value for pulse time which yields higher growth rate with a relatively higher material usage efficiency.

Figure 9 shows the effects of purge time on the process wastes and emissions at three levels (5 s, 10 s and 15 s) with 0.02 s pulse time at 200°C and 30 sccm carrier gas flow rate. The effect of purge time on precursor dosage is very weak as shown in Fig.9 (a), while it increases the precursor waste especially from 5 s purging time to 10 s. With longer purge time, more precursor residuals in the chamber are purged by the carrier gas. As the majority of precursor residuals are cleaned within 10 s, there is no evident increase in the precursor wastes with 15 s purge.

Methane emissions are increased from 5 s purge time to 10 s and a slightly increment is seen at 15 s as shown in Fig.9 (a). The similar effect of purge time on material deposition rate is observed in Fig.9 (b). Methane generation is positively related to the material deposition process, and longer purge time implies more surface reactions on the substrate surface due to the longer contact of precursor molecules with the surface sites. As a result, the growth rate is increased from 1.15 Å/cycle with 5 s purge time to 1.17 Å/cycle with 10 s.

When the purge process is further prolonged to 15 s, the growth rate is seen at the same level as 10 s. This is mainly due to the fact that in the first 10 s, the majority of the reactive surface species has been consumed. Lack of reactive surface species has inhibited the material chemisorption. The material waste rate shown in Fig.9 (b) is higher in longer purge process. From the results in Fig.9, shorter purge process, e.g., 5 s, generates fewer precursor wastes, but also results in lower growth rate. With both deposition throughput and sustainability performance taken into account, 10 s might be the optimal choice for the purge time.

Carrier gas flow rate affects the surface deposition process and emissions by enhancing the convective heat and mass transfer in ALD system as revealed by Fig.10, in which three

levels of carrier gas flow rate 10, 20 and 30 sccm are investigated with 0.02/10/0.02/10 s ALD cycle at 200°C chamber temperature. As shown in Fig.10 (a), precursor wastes increase with higher flow rate. Total precursor wastes gathered from the outlet increase from 0.13 mg/cycle with 10 sccm flow rate to 0.18 mg/cycle with 30 sccm. Higher carrier gas flow rate shortens the contact time of precursors with substrate surface, and thus more unreacted precursor materials are carried out of the system.

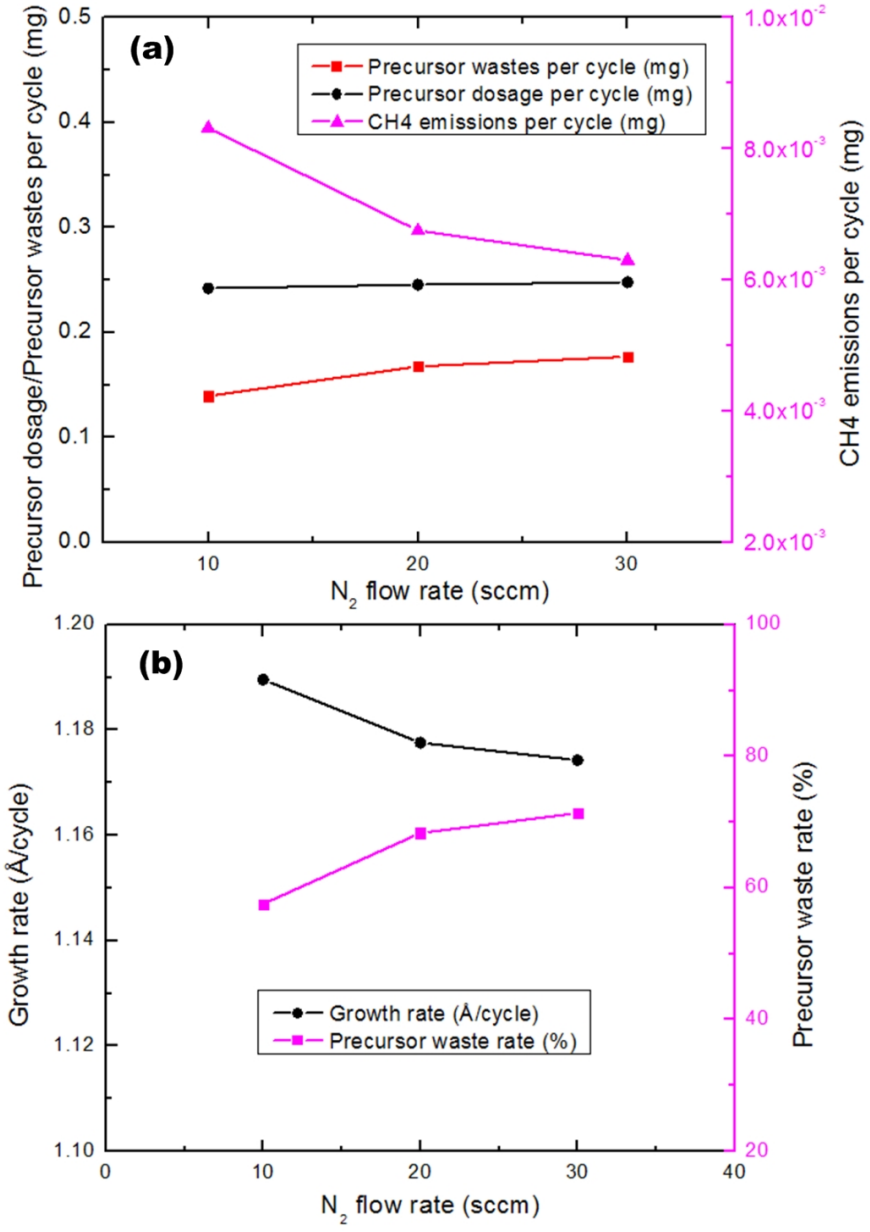

Fig.10 Effects of carrier gas flow rate on the process wastes and emissions (a) precursor dosage, precursor wastes and methane emissions and (b) film growth rate and precursor waste rate

As more unreacted precursor materials are purged by higher N_2 flow rate, less surface reaction is resulted in due to lower gaseous precursor concentrations on the wafer surface. The growth rate is decreased from 1.19 Å/cycle with 10 sccm carrier gas flow rate to 1.17 Å/cycle

with 30 sccm. Methane emission also decreases due to the weakened surface reactions. Because more precursor molecules are purged out without reacting with the surface species on substrate, the precursor waste rate is seen higher at higher flow rate in Fig.10 (b). From the results presented in Fig.10, lower carrier gas flow rate, e.g., 10 sccm is desirable to achieve higher growth rate, and meanwhile restrain the precursor waste rate.

5 Conclusions

This paper systematically studied the transient deposition process and sustainability performance with the aid of DFT calculations of the Al_2O_3 ALD reaction mechanism. The detailed ALD surface reaction mechanism including 10 elementary surface reactions in Al_2O_3 ALD process was examined and developed based on the DFT atomic-level investigations. The improved surface reaction mechanism with accurate kinetic data was coupled and integrated in the physical thermal-fluid model. Using the numerical model, the transient deposition process was studied and analyzed by probing the distribution variations of the gaseous, surface and bulk species in a full Al_2O_3 ALD cycle. The full-cycle ALD simulation revealed that the depositions of bulk material in ALD are in essence the chemisorption of the gaseous species and the conversion of surface species. The actual deposition process is heavily dependent on the interactions of these various species, which are essentially influenced by the process parameters.

To explore the effects of the four process parameters of temperature, pulse and purge procedures as well as the carrier gas flow rate on material deposition, process wastes and emissions, film growth rate on Si substrate was characterized, and methane emissions were gathered in both actual ALD system and numerical simulation. It is found by the studies that ALD process has very high material waste rate, and ~ 60% precursor dosage is wasted. It is also concluded that methane emission is positively proportional to the film deposition process. Temperature fundamentally affects the ALD chemical process by changing the energy states in the surface reactions. Both experimental and numerical results show that moderate chamber temperature of 200°C results in higher growth rate and fewer precursor waste. Too high temperature decreases the film growth rate by enhancing the decomposition process.

Pulse time is directly related to the precursor dosage. Longer pulse time enhances the deposition process, but also increases the precursor waste which as a result weakens the

sustainability performance. Purge time and carrier gas flow rate have very weak influences on deposition process, wastes and emissions. Purge time influences the ALD process by changing the gas-surface interacting time, and high carrier gas flow rate alters the ALD flow field by enhancing the convective heat and mass transfer in ALD process. The effects of the process parameters must be considered by minimizing the process wastes and emissions while maintaining a high deposition rate. In many cases, a trade-off must be made in defining the optimal process parameters.

As ALD is on a rapid expansion to more applications, its sustainability issues are standing out. This study relies on the theoretical DFT calculations to study the sustainability performance of the Al_2O_3 ALD process. Fundamental experimental investigations are strongly needed in understanding the transient ALD deposition process, that can provide verifying evidences for theoretical studies. The reactive thermal-fluid dynamic model in this study will be more accurate in characterizing the ALD deposition and emission process with such experimental data. In the meantime, novel and effective in-situ nano-particle investigation approaches need to be developed to study the formations of nano-wastes and nano-particles in ALD process.

Acknowledgement

Financial support from National Science Foundation (CMMI-1200940) is gratefully acknowledged.

References

[1] George, S. M., 2010, "Atomic Layer Deposition: An Overview," Chem. Rev., 110(1), pp. 111-131.

[2] Groner, M. D., Fabreguette, F. H., Elam, J. W., and George, S. M., 2004, "Low-temperature Al2O3 atomic layer deposition," Chem. Mater., 16(4), pp. 639-645.

[3] Scarel, G., Ferrari, S., Spiga, S., Wiemer, C., Tallarida, G., and Fanciulli, M., 2003, "Effects of growth temperature on the properties of atomic layer deposition grown ZrO2 films," J. Vac. Sci. Technol., A, 21(4), pp. 1359-1365.

[4] Hsueh, Y. C., Wang, C. C., Kei, C. C., Lin, Y. H., Liu, C., and Perng, T. P., 2012, "Fabrication of catalyst by atomic layer deposition for high specific power density proton exchange membrane fuel cells," J. Catal., 294, pp. 63-68.

[5] Narayan, R. J., Adiga, S. P., Pellin, M. J., Curtiss, L. A., Hryn, A. J., Stafslien, S., Chisholm, B., Shih, C. C., Shih, C. M., Lin, S. J., Su, Y. Y., Jin, C. M., Zhang, J. P., Monteiro-Riviere, N. A., and Elam, J. W., 2010, "Atomic layer deposition-based functionalization of materials for medical and environmental health applications," Philosophical Transactions of the Royal Society a-Mathematical Physical and Engineering

Sciences, 368(1917), pp. 2033-2064.
[6] Niu, W., Li, X., Karuturi, S. K., Fam, D. W., Fan, H., Shrestha, S., Wong, L. H., and Tok, A. I. Y., 2015, "Applications of atomic layer deposition in solar cells," Nanotechnology, 26(6), p. 064001.
[7] Shu, T., Liao, S. J., Hsieh, C. T., Roy, A. K., Liu, Y. Y., Tzou, D. Y., and Chen, W. Y., 2012, "Fabrication of platinum electrocatalysts on carbon nanotubes using atomic layer deposition for proton exchange membrane fuel cells," Electrochim. Acta, 75, pp. 101-107.
[8] Skoog, S. A., Elam, J. W., and Narayan, R. J., 2013, "Atomic layer deposition: medical and biological applications," Int. Mater. Rev., 58(2), pp. 113-129.
[9] Yu, M. P., Yuan, W. J., Li, C., Hong, J. D., and Shi, G. Q., 2014, "Performance enhancement of a graphene-sulfur composite as a lithium-sulfur battery electrode by coating with an ultrathin Al2O3 film via atomic layer deposition," Journal of Materials Chemistry A, 2(20), pp. 7360-7366.
[10] Pan, D., Ma, L., Xie, Y., Jen, T. C., and Yuan, C., 2015, "On the physical and chemical details of alumina atomic layer deposition: A combined experimental and numerical approach," J. Vac. Sci. Technol., A, 33(2).
[11] Pan, D. Q., Li, T., Jen, T. C., and Yuan, C., 2014, "Numerical modeling of carrier gas flow in atomic layer deposition vacuum reactor: A comparative study of lattice Boltzmann models," J. Vac. Sci. Technol., A, 32(1).
[12] Xie, Y., Ma, L., Pan, D., and Yuan, C., 2015, "Mechanistic modeling of atomic layer deposition of alumina process with detailed surface chemical kinetics," Chem. Eng. J., 259(0), pp. 213-220.
[13] Pan, D., Ma, L., Xie, Y., Wang, F., Jen, T.-C., and Yuan, C., 2015, "Experimental and numerical investigations into the transient multi-wafer batch atomic layer deposition process with vertical and horizontal wafer arrangements," Int. J. Heat Mass Transfer, 91, pp. 416-427.
[14] Yuan, C. Y., and Dornfeld, D., 2008, "Environmental performance characterization of atomic layer deposition," Electronics and the Environment, 2008. ISEE 2008. IEEE International Symposium on, pp. 1-6.
[15] Yuan, C. Y., and Dornfeld, D. A., 2010, "Integrated Sustainability Analysis of Atomic Layer Deposition for Microelectronics Manufacturing," Journal of Manufacturing Science and Engineering-Transactions of the Asme, 132(3).
[16] Ma, L., Pan, D., Xie, Y., and Yuan, C., 2015, "Atomic layer deposition of Al2O3 process emissions," RSC Advances, 5(17), pp. 12824-12829.
[17] Remmers, E. M., Travis, C. D., and Adomaitis, R. A., 2015, "Reaction factorization for the dynamic analysis of atomic layer deposition kinetics," Chem. Eng. Sci., 127, pp. 374-391.
[18] Widjaja, Y., and Musgrave, C. B., 2002, "Quantum chemical study of the mechanism of aluminum oxide atomic layer deposition," Appl. Phys. Lett., 80(18), pp. 3304-3306.
[19] Halls, M. D., and Raghavachari, K., 2004, "Atomic layer deposition growth reactions of Al2O3 on Si(100)-2 x 1," J. Phys. Chem. B, 108(13), pp. 4058-4062.
[20] Elliott, S. D., and Greer, J. C., 2004, "Simulating the atomic layer deposition of alumina from first principles," J. Mater. Chem., 14(21), pp. 3246-3250.
[21] Delabie, A., Sioncke, S., Rip, J., Van Elshocht, S., Pourtois, G., Mueller, M., Beckhoff, B., and Pierloot, K., 2012, "Reaction mechanisms for atomic layer deposition of aluminum oxide on semiconductor substrates," J. Vac. Sci. Technol., A, 30(1).
[22] Hass, K. C., Schneider, W. F., Curioni, A., and Andreoni, W., 1998, "The chemistry of water on alumina surfaces: Reaction dynamics from first principles," Science, 282(5387), pp. 265-268.
[23] Halls, M. D., and Raghavachari, K., 2003, "Atomic layer deposition of Al2O3 on H-passivated Si. I. Initial surface reaction pathways with H/Si(100)-2X1," J. Chem. Phys., 118(22), pp. 10221-10226.
[24] Steinfeld, J. I., Francisco, J. S., and Hase, W. L., 1999, Chemical Kinetics and Dynamics, Prentice Hall.
[25] Atkins, P., and de Paula, J., 2011, Physical Chemistry for the Life Sciences, W. H. Freeman.
[26] Chang, R., 2005, Physical Chemistry for the Biosciences, University Science Books.
[27] Davis, M. E., and Davis, R. J., 2012, Fundamentals of Chemical Reaction Engineering, Dover Publications.

[28] Tompkins, H., and Irene, E. A., 2005, Handbook of Ellipsometry, Elsevier Science.